Single cobalt atom anchored black phosphorous nanosheets as an effective cocatalyst promotes photocatalysis

Xiaohui Ren,[a, b] Li Shi,*[b] Yunxiang Li,[a, b] Shuang Song,[b, c] Qi Wang,[a, b] Shunqin Luo,[a, b] Long Ren,[d] Hongwei Zhang,[e] Yasuo Izumi,[e] Xinsheng Peng,[f] Davin Philo,[a, b] Fumihiko Ichihara,[a, b] Jinhua Ye*[a, b, g, h]

[a] X. Ren, Dr. Y. Li, Q. Wang, S. Luo, D. Philo, F. Ichihara, Prof. Dr. J. Ye
Graduate School of Chemical Sciences and Engineering
Hokkaido University
Kita 8, Nishi 5, Kita-ku
Sapporo 060-0814 (Japan)

[b] X. Ren, Dr. L. Shi, Dr. Y. Li, S. Song, Q. Wang, S. Luo, D. Philo, F. Ichihara, Prof. Dr. J. Ye
International Center for Materials Nanoarchitectonics (WPI-MANA)
National Institute for Materials Science (NIMS)
1-1 Namiki, Tsukuba
Ibaraki 305-0044 (Japan)
E-mail: SHI.Li@nims.go.jp (Dr. L. Shi); Jinhua.YE@nims.go.jp (Prof. Dr. J. Ye)

[c] S. Song
Department of Environmental Science and Engineering
School of Architecture and Environment
Sichuan University
Chengdu 610065 (P. R. China)

[d] Dr. L. Ren
Australia Institute for Superconducting and Electronic Materials (ISEM)
Australian Institute for Innovative Materials (AIIM)
University of Wollongong
Wollongong NSW 2500 (Australia)

[e] H. Zhang, Prof. Dr. Y. Izumi
Department of Chemistry
Graduate School of Science
Chiba University
Yayoi 1-33, Inage-Ku
Chiba 263-8522 (Japan)

[f] Prof. Dr. X. Peng
State Key Laboratory of Silicon Materials
School of Materials Science and Engineering
Zhejiang University
Hangzhou 310027 (P. R. China)

[g] Prof. Dr. J. Ye
TJU-NIMS International Collaboration Laboratory

School of Material Science and Engineering
Tianjin University
Tianjin 300072 (P. R. China)
[h] Prof. Dr. J. Ye
Collaborative Innovation Center of Chemical Science and Engineering (Tianjin)
Tianjin 300072 (P. R. China)

Section 1. Experimental section

Structural characterizations. The atomic structural information of the sample was determined by X-ray diffraction (XRD, PANalytical X'Pert PRO). Raman spectra were collected by engaging the Raman microscope (NRS-1000, Japan) with 532 nm excitation at room temperature. The surface morphologies of the samples were performed on the field emission scanning electron microscopy (FE-SEM, JSM-6701F). High resolution scanning TEM (STEM) images, and STEM-energy dispersive X-ray spectroscopy (EDX) images were obtained using a JEOL ARM-200CF operated at 200 kV with an X-ray collection angle of ~1 sr. The EDX elemental map was obtained using NSS 3.3.94 Noran System Seven software, in which principal component analysis can be performed to identify regions with a similar composition within a map. Atomic force microscopy (AFM) measurements were employed on (Nanocute H, Japan) to acquire the thickness of 2D BP nanosheets. UV-Vis absorption spectra were recorded by Ultraviolet-visible spectroscopy (UV-vis, UV-2600 Shimadzu Corp., Japan), the bandgap can be calculated according to transformed Kubelka-Munk function. Zeta-potential analysis was conducted on Zetasizer Nano ZS 90 (Malvern, UK). The surface chemical analysis was conducted on X-ray photoelectron spectroscopy (XPS, VG-ESCA Mark II). The decay time measurements were performed on a Hamamatsu instrument (Hamamatsu C5680, Japan).

X-ray absorption spectroscopy. Co K-edge X-ray absorption fine structure (XAFS) spectra were measured at 290 K in the transmission mode in the Photon Factory Advanced Ring at the High Energy Accelerator Research Organization on beamline 9C. The storage ring energy was 2.5 GeV, and the ring current was 450 mA. A Si (1 1 1) double-crystal monochromator and Rh-coated focusing bent cylindrical mirror were inserted into the X-ray beam path. The X-ray intensity was suppressed to 67% of the maximum flux using a piezo-translator applied to the crystal to suppress higher harmonics. The slit in front of the I_0 ionization chamber had an opening size of 1.0 mm (vertical) 2.0 mm (horizontal). For comparison, Co metal foil, CoO, and CoP on analytical grade were used as reference materials. The data analysis was carried out for cobalt speciation, including the oxidation state and the chemical environment surrounding the atoms. The X-ray energy was calibrated with reference to the first inflection point in the spectrum of Co foil (7709.5 eV). The disks (Φ = 10 mm) were formed by diluting the CoO (11 mg),

BP-Co (10 mg) and CoP (10 mg) with boron nitride (30 mg) and measured at the beamline. X-ray absorption spectra were analyzed using the ATHENA program in IFEFFIT package. Pre-edge background was subtracted by a linear equation that was fitted to the region below the absorption edge, while the post-edge background was also subtracted by fitting a polynomial quadratic function to the EXAFS region. The processed data were normalized by cubic spline method. Extended X-ray absorption fine structure (EXAFS) spectra were analyzed in the conventional procedure with the aid of ATHENA and ARTEMIS program in IFEFFIT package. EXAFS oscillations, $\chi(k)$, were extracted from the spectra in the procedure above and transformed from angular wave number k-space (k^3, k_{min} = 2.3 Å^{-1}, k_{max} = 8.2 Å^{-1}) using a Hanning window to interatomic distance R-space to obtain the radial structure function (RSF). The EXAFS spectrum for the first shell was extracted by the inverse Fourier Transform of the RSF over the appropriate region, and data fitting was performed using the single scattering EXAFS equation in both k- and R-space. The amplitude and phase shift functions for Co-O and Co-P shells were extracted using a code ARTEMIS from the EXAFS data measured for CoO and CoP.

Photoelectrochemical (PEC) measurements. The PEC measurements were performed in an integrated functional system equipped with a standard three-electrode system, where working electrode was adopted as photoanode and counter electrode (Platinum wire) was used as cathode. Meanwhile, 0.5 M Na_2SO_4 (pH=7) solution were used as electrolytes, and a Ag/AgCl electrode was adopted as the reference electrode. Electrochemistry workstation CHI660D (CH Instruments, Inc., Shanghai) was used to control the bias potential and record the photocurrent generated. The simulated solar light source was placed 20 cm away from the reaction vessel and the illumination intensity on the photoanode was fixed at 100 mW cm^{-2}. Amperometric i-t curves were evaluated under bias potential 0.5 V. The response time ($t_{res.}$) and recovery time ($t_{rec.}$) can be assigned into the time intervals for the rise and decay of photocurrent from 10 % to 90 % and from 90 % to 10 % of its peak value. The Electrochemical Impedance Spectrum (EIS) measurements were conducted at their open-circuit potential, with the frequency range of 100 kHz to 0.01 Hz and perturbation amplitude of 5 mV. The Mott-Schottky plots were acquired under applied alternating current (AC) frequency is 1000 Hz. All the experiments were carried out at the same condition.

Section 2. Characterization results.

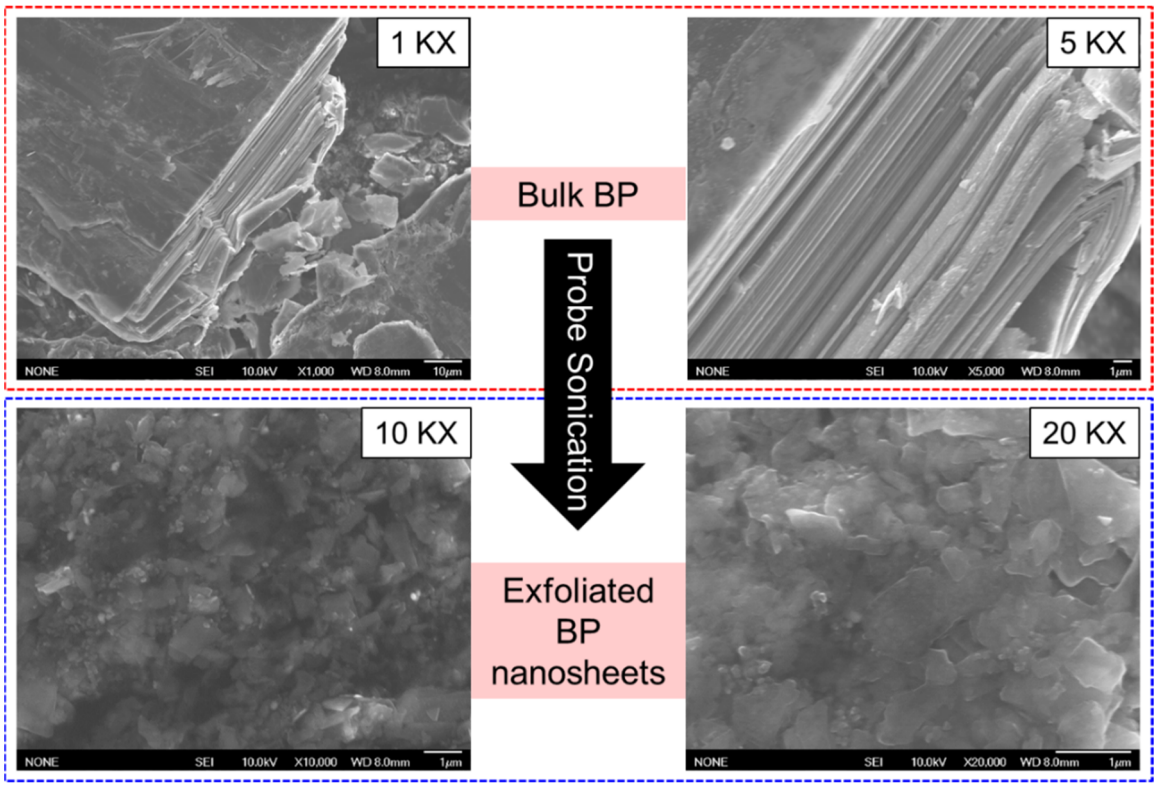

Figure S1. SEM images of (a) and (b) bulk black phosphorous crystal used as received, (c) and (d) as-exfoliated two-dimensional black phosphorous nanosheets.

Discussion: Few-layer BP nanosheets synthesized from bulk BP powder by a facile liquid exfoliation method. BP crystals that re-stacked by a sequence of layer structures are shown in Figure S1 (a) and (b), while Figure S1 (c) and (d) demonstrate BP nanosheets with uniformly distributed lateral dimension after liquid exfoliation. BP nanosheets are found to show intact lamellar structure after sonication procedures, and the morphology of BP nanosheets can be distinctly distinguished.

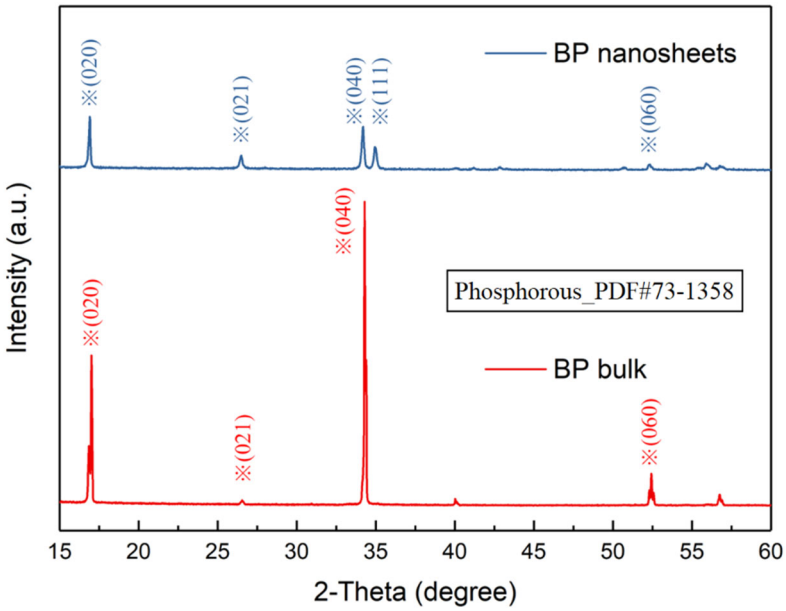

Figure S2. XRD patterns of BP bulk and BP nanosheets.

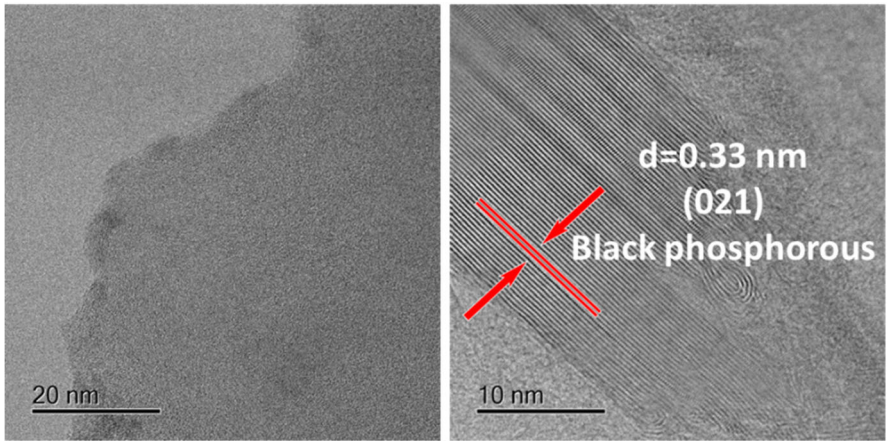

Figure S3. TEM and HRTEM images of few-layer BP nanosheets, the lattice spacing (d-spacing) 0.33 nm is corresponding to (021) planes of BP.

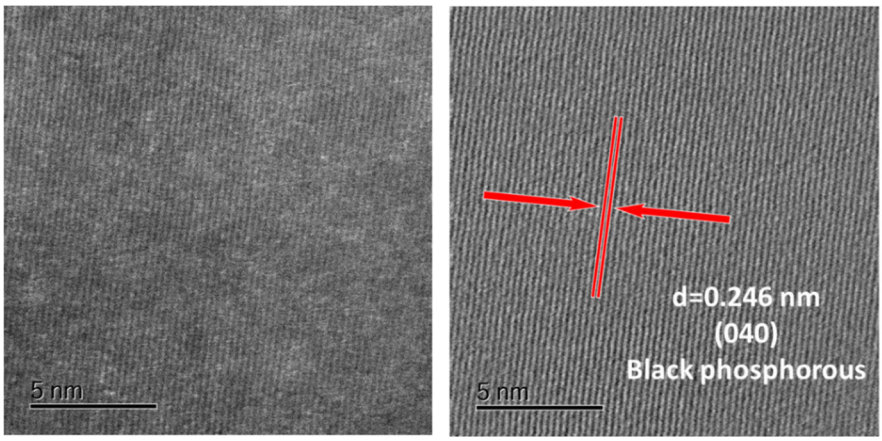

Figure S4. Additional TEM and HRTEM images of few-layer BP nanosheets, the lattice spacing (d-spacing) 0.246 nm is corresponding to (040) plane of BP.

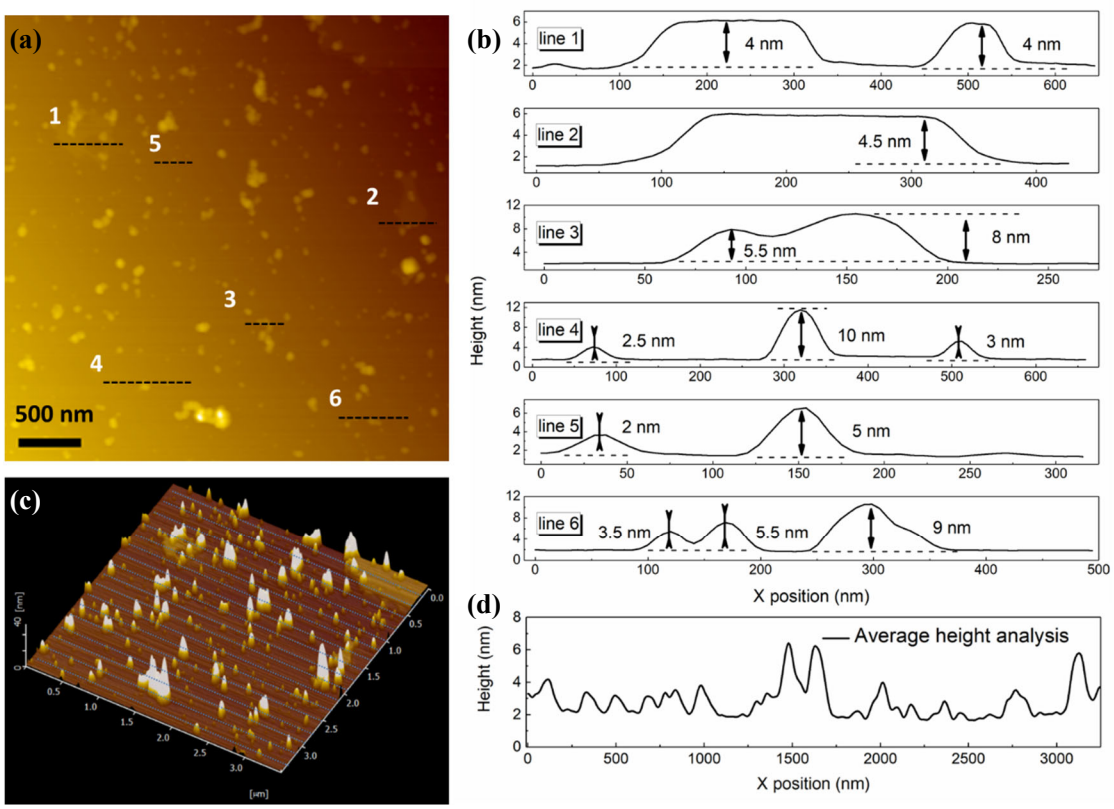

Figure S5. (a) Tapping-mode AFM image and (b) the related cross-sectional analysis (line 1 to line 6) of exfoliated BP nanosheets. (c) Average line analysis and (d) the corresponding height profile of exfoliated few-layer BP nanosheets.

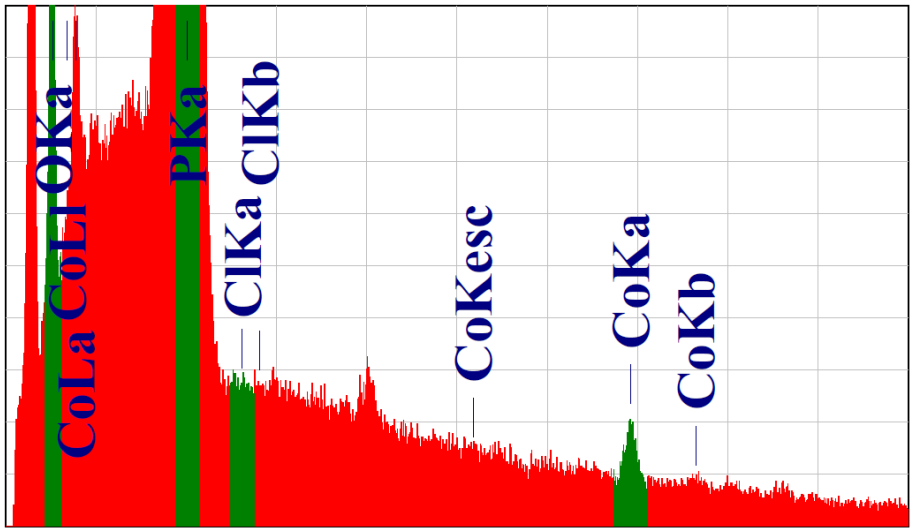

Figure S6. Energy-dispersive X-ray spectroscopy of BP-Co.

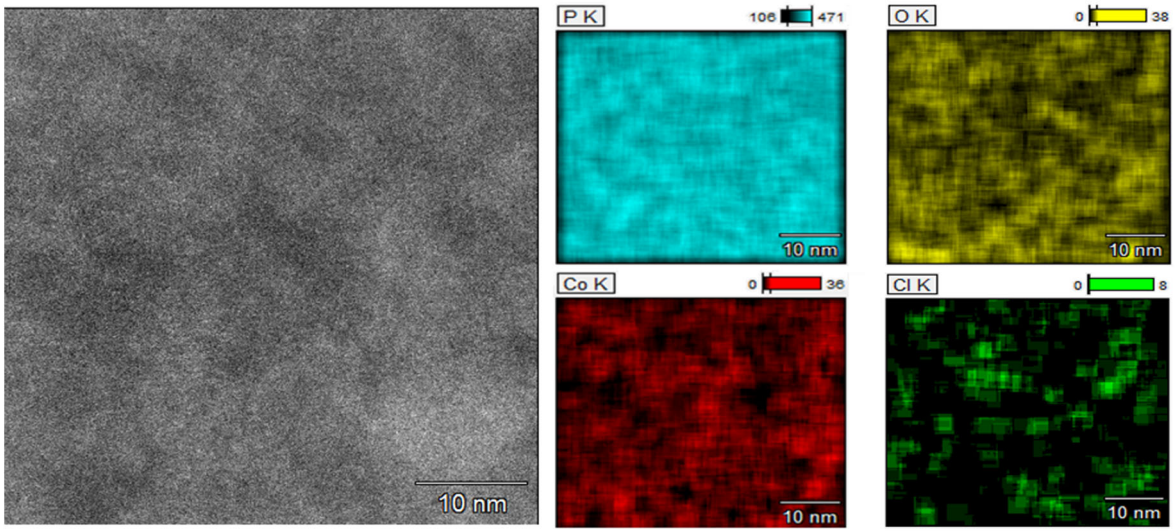

Figure S7. TEM image and relevant EDS mapping of elements P, O, Co and Cl from the selected area of BP-Co material.

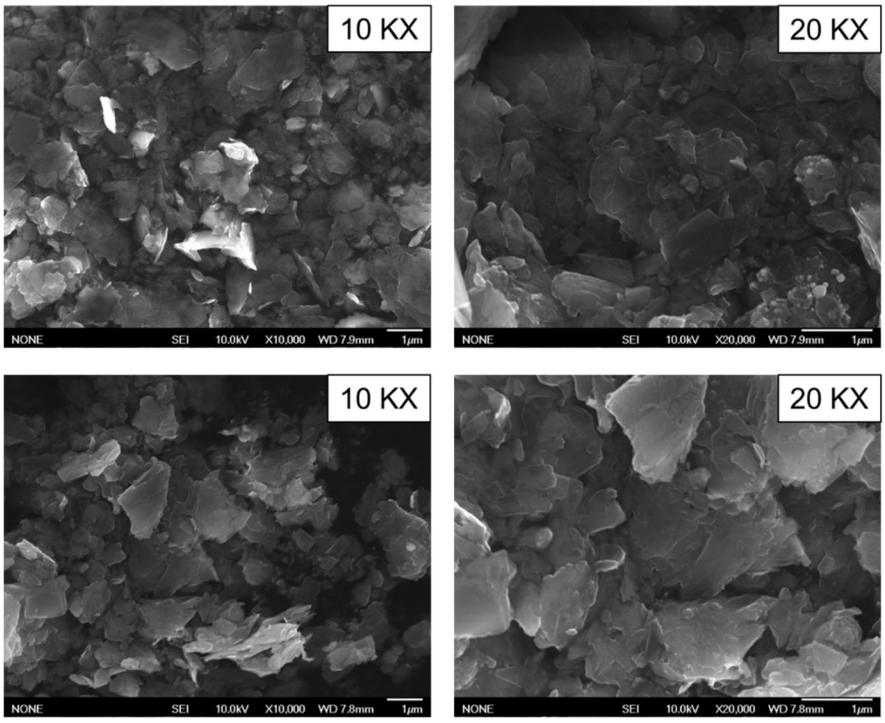

Figure S8. Low (left) and high (right) resolution SEM images of BP nanosheets after Co loading.

Discussion: The lone pair electrons in BP atom structure are thermodynamics unstable, preferring to establish stable bond with Co^{2+} spontaneously (detail explanations are provided in the main article). Both SEM and TEM images show the layer structure of BP nanosheets is preserved after loading with Co, and also a strong interaction between P and Co can prove the successful Co loading on the surface of BP nanosheets.

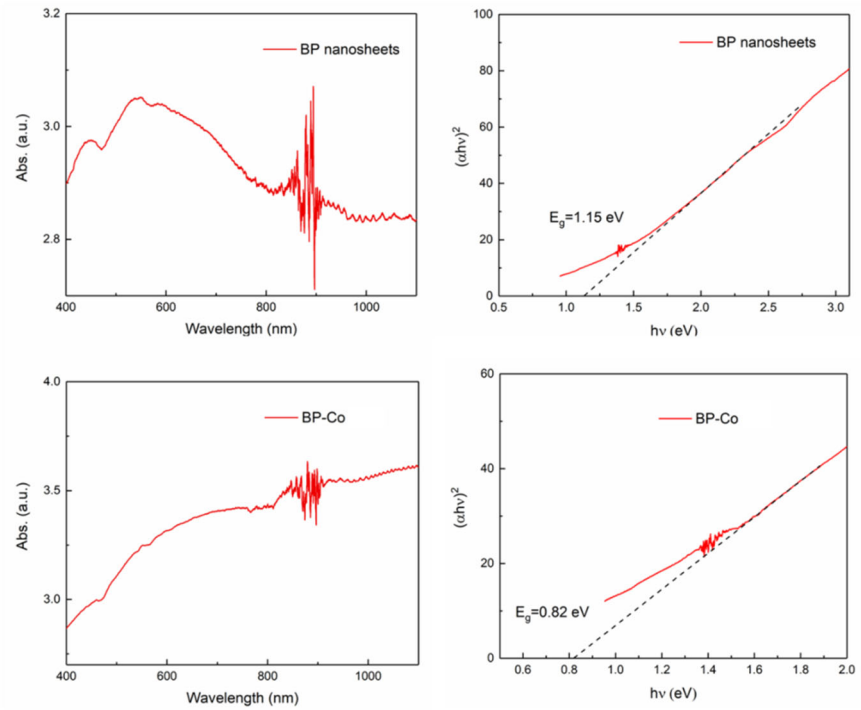

Figure S9. Apparent bandgaps of as-exfoliated BP nanosheets and BP-Co determined from UV-Vis absorption spectra.

Discussion: As shown in Figure S9, the bandgap of BP and BP-Co can be determined from the threshold value of intrinsic absorption edge (1078 nm for BP and 1512 nm for BP-Co) to be 1.15 eV and 0.82 eV, respectively. A narrowed bandgap from 1.15 eV to 0.82 eV can be observed. This change is resulted from the formation of Co-P(O) on BP nanosheets surface, which lead to form intermediate energy states and act as trap sites to accommodate the photogenerated electrons as well as promote charge carrier migration in consequence.

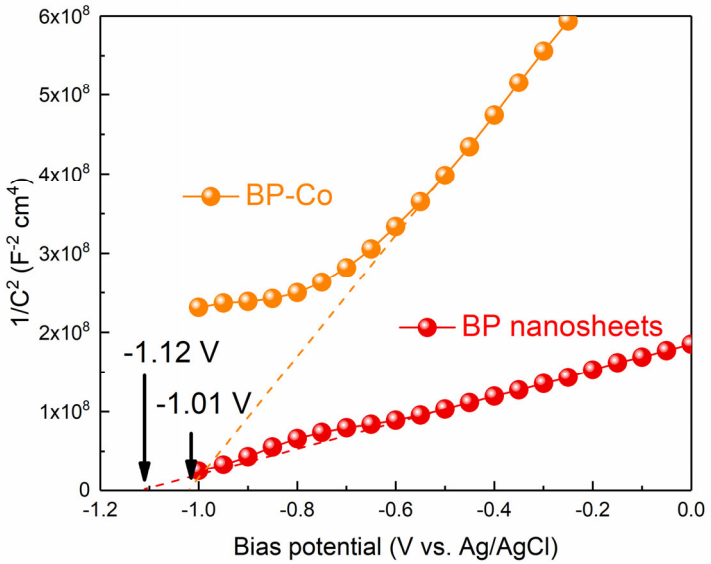

Figure S10. Mott-Schottky plot of as-exfoliated BP nanosheets and BP-Co.

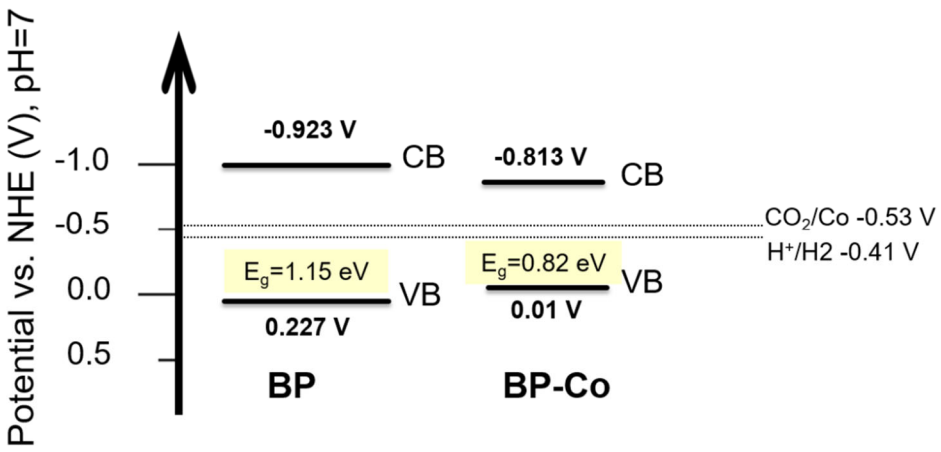

Figure S11. Schematic band structure diagram of as-exfoliated BP nanosheets and BP-Co.

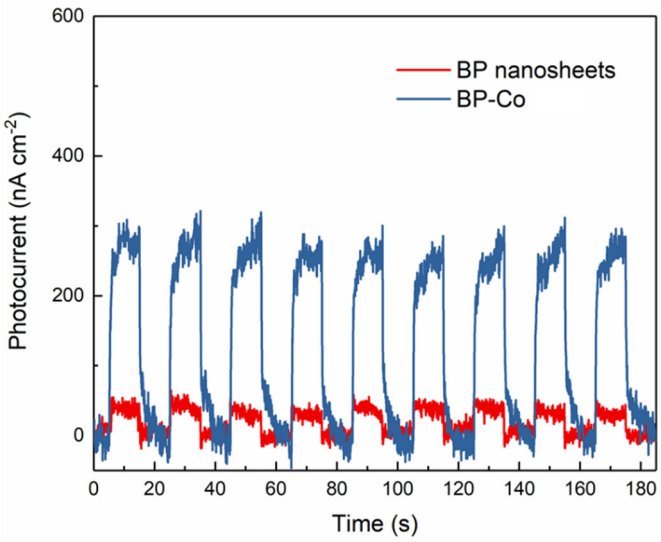

Figure S12. Photocurrent response behaviors of as-exfoliated BP nanosheets and BP-Co.

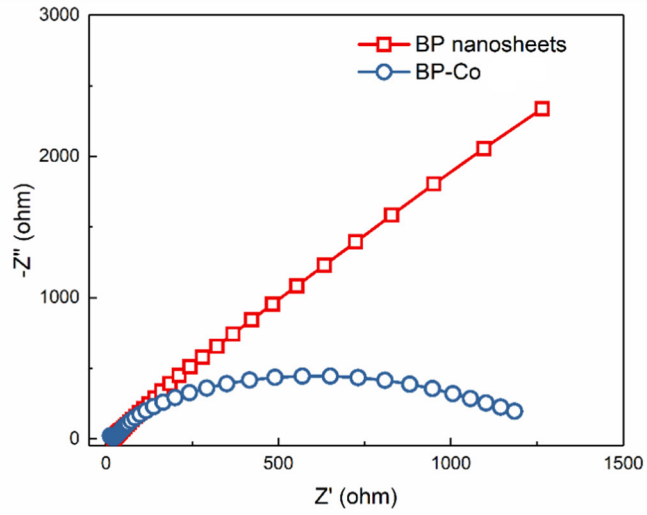

Figure S13. EIS plots of as-exfoliated BP nanosheets and BP-Co.

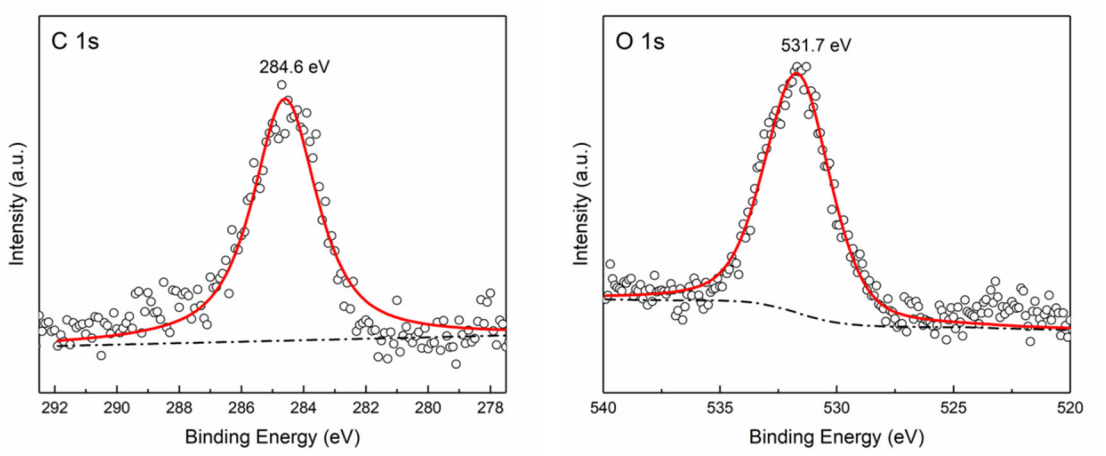

Figure S14. Fitting C 1s and O 1s characteristic peaks of BP nanosheets for calibration.

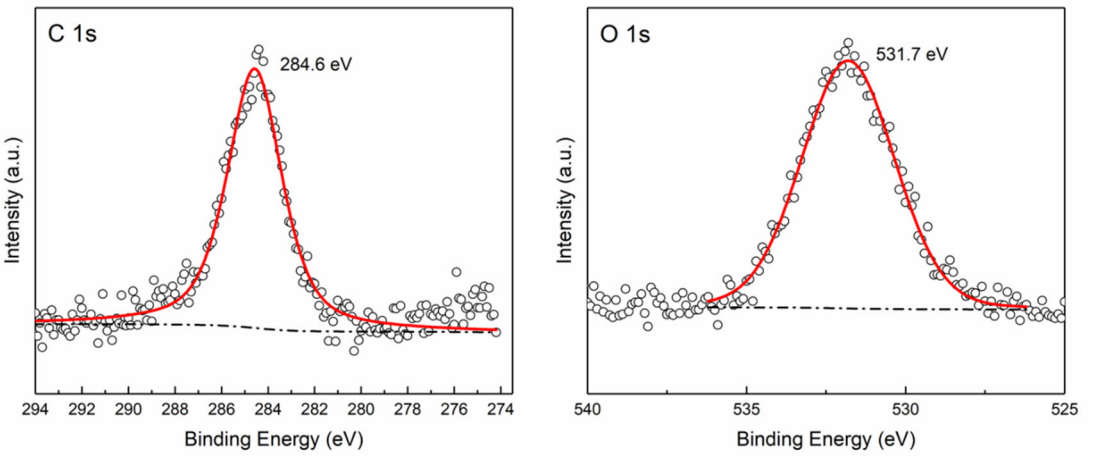

Figure S15. Fitting C 1s and O 1s characteristic peaks of BP-Co nanosheets for calibration.

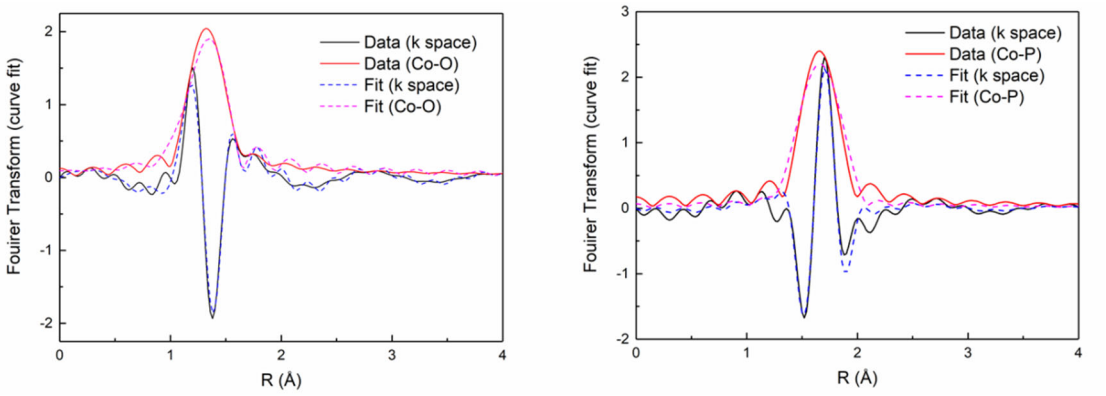

Figure S16. The best-fit results in k and R-space for Co-O and Co-P for BP-Co associated Fourier transform k^3-weighted EXAFS spectra.

Section 3. Photocatalytic H_2 evolution performance on CdS-BP-Co materials.

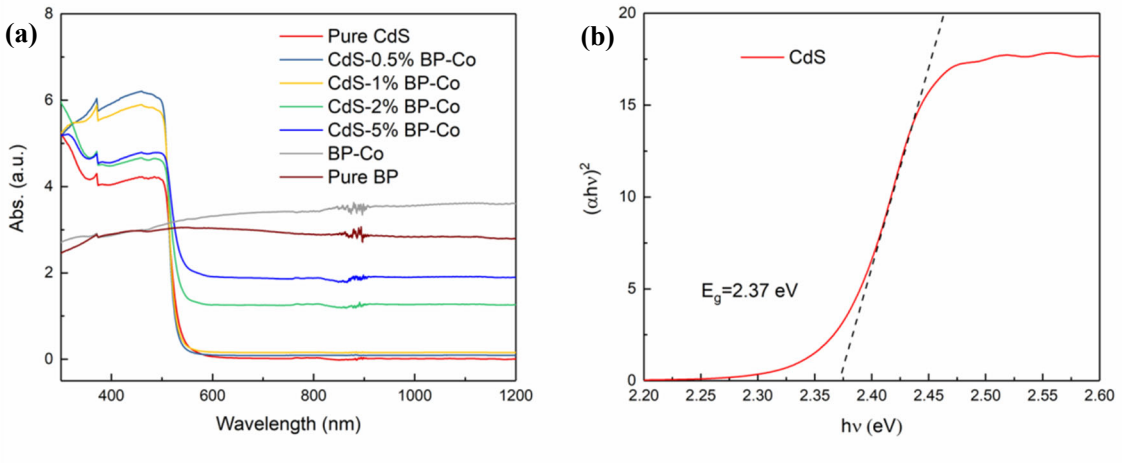

Figure S17. (a) UV-Vis diffuse reflectance spectra of pure CdS, CdS with 0.5 wt%-5 wt% BP-Co, BP-Co and pure BP. (b) Intrinsic absorption edge of CdS with the bandgap calculated to be 2.37 eV through transformed Kubelka-Munk function.

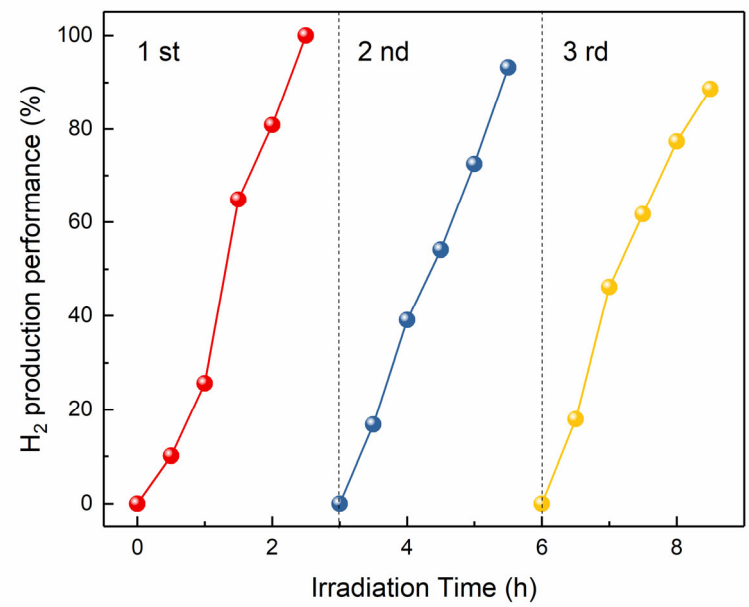

Figure S18. Stability test of CdS-1 wt % BP-Co for photocatalytic H_2 production.

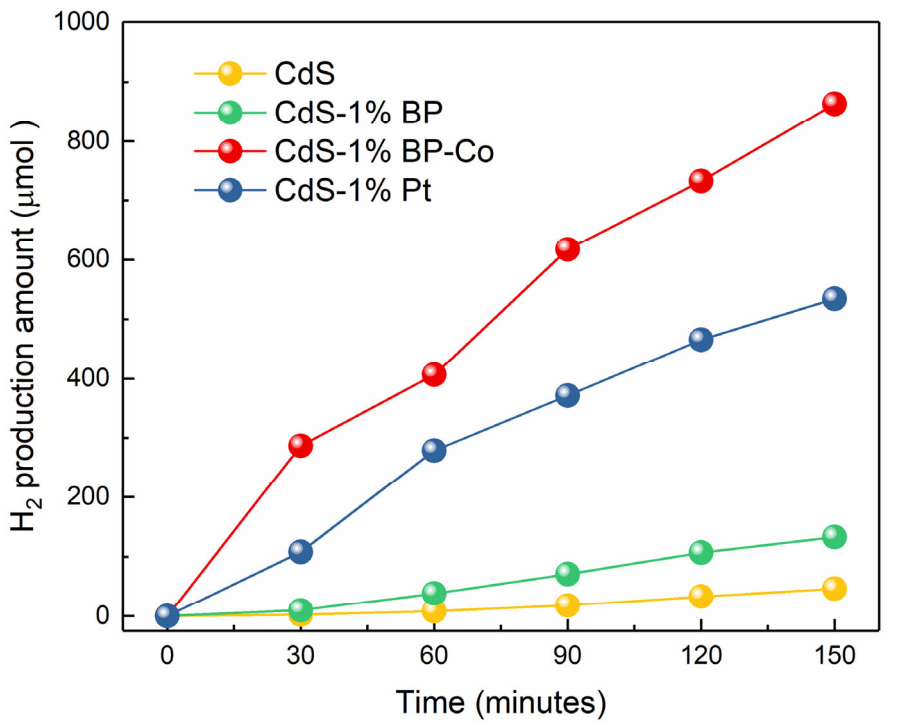

Figure S19. Plots of H_2 production amount within 2.5 hours of CdS, CdS-1 wt% BP, CdS-1 wt% BP-Co and CdS-1 wt% Pt.

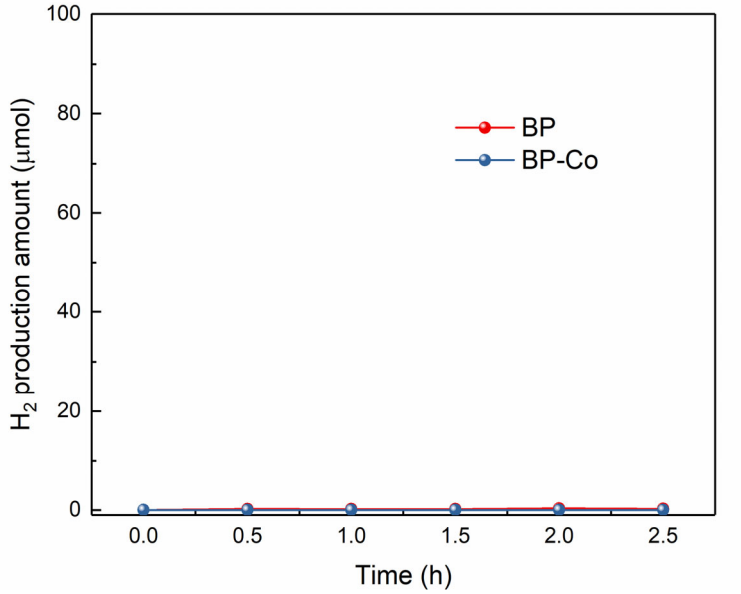

Figure S20. H_2 production amount within 2.5 hours of BP and BP-Co.

Section 3. Photocatalytic H_2 evolution performance on EY sensitized BP-Co.

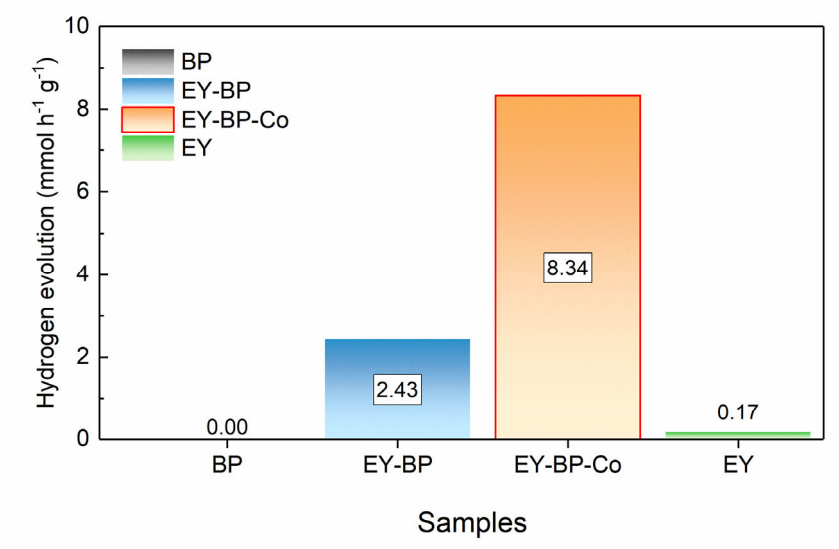

Figure S21. Hydrogen evolution performance comparison of BP, EY-BP, EY-BP-Co, and BP-Co EY materials.

In Figure S21, bare BP nanosheets hardly show H_2 production ability. With the contribution from photosensitizer Eosin Y, a great enhancement of water reduction ability (H_2 production about 24.3 μmol h^{-1}) can be achieved by BP nanosheets. The H_2 production as high as 83.4 μmol h^{-1} (8.34 mmol h^{-1} g^{-1}) is achieve by BP-Co.

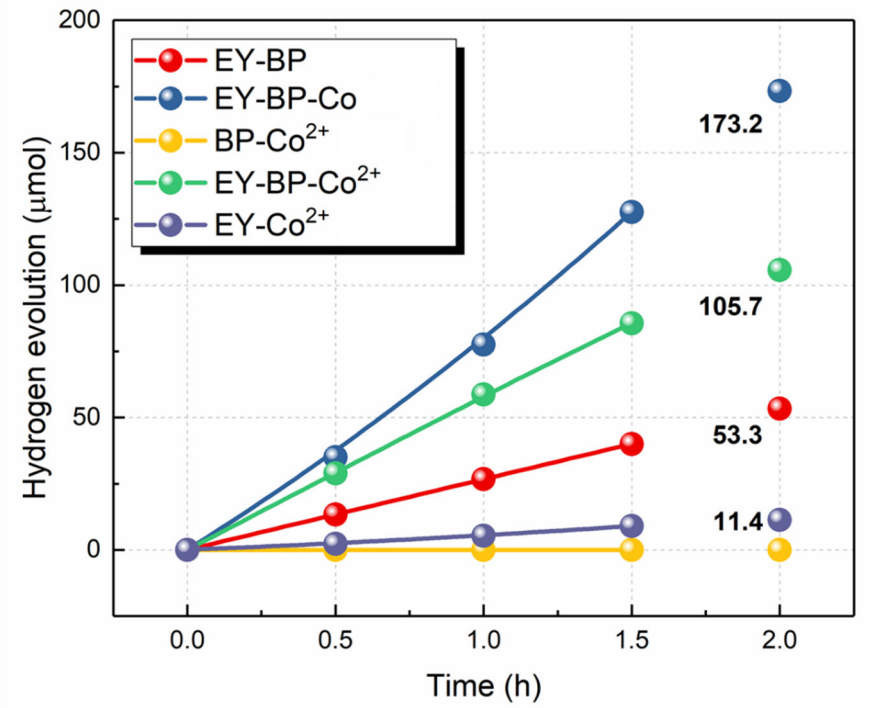

Figure S22. H_2 production amount within 2 hours of five different samples based on BP, BP-Co and BP-Co^{2+}. BP-Co^{2+} was prepared by mixing BP with $CoCl{\cdot}6H_2O$ (same Co amount) in ethanol and dried without annealing.

We also conduct a series of comparison experiments in proving the importance of BP-Co interaction. Figure S22 demonstrates the H_2 production amount within 2 hours of five different samples based on BP, BP-Co and BP-Co^{2+}. The H_2 production performance of Co^{2+} is negligible, even with the introduction of BP nanosheets, the ultimate H_2 production can only reach one-half of that of BP-Co after annealing.

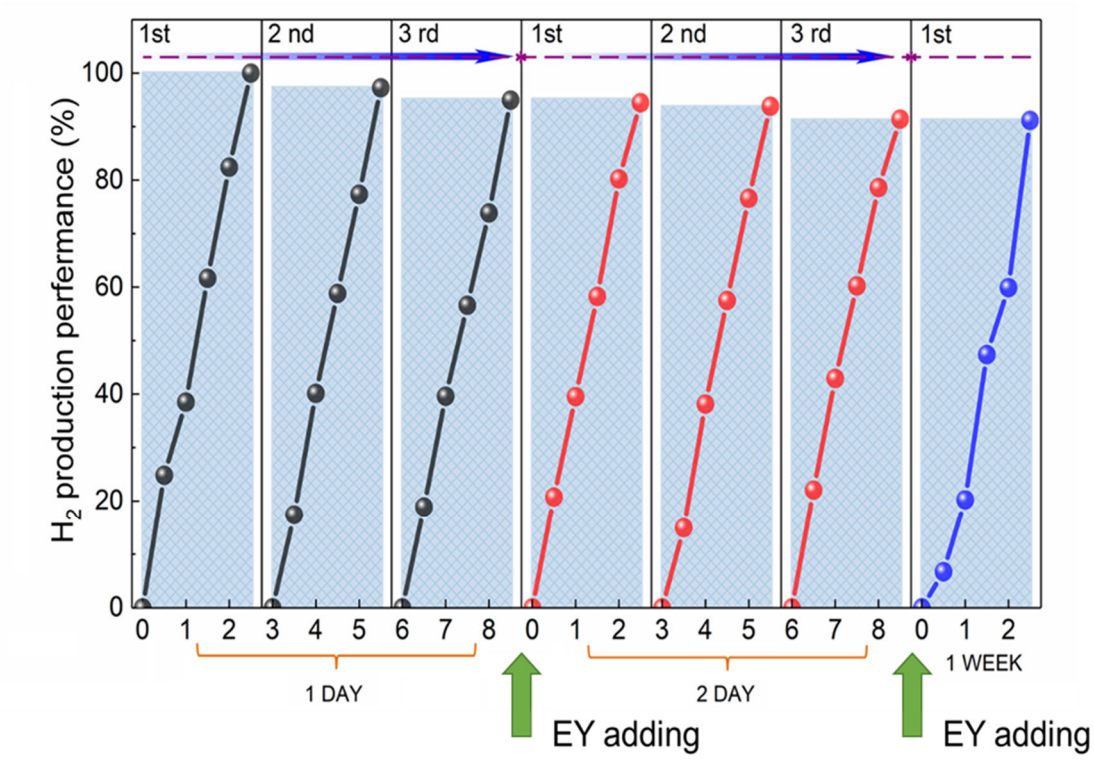

Figure S23. Cycling test of H_2 evolution performance over BP-Co.

The cycle measurements have been carried out to evaluate the durability of BP photocatalyst. As shown in Figure S23, the H_2 production amount depict no distinct decay in the first round, and only a slight reduce on the performance can be find in second and third rounds, which may be induce by decreasing of sacrificial agent and EY. After resupplying the EY, the photocatalytic performance retains after one day, and the activity retain 90 % from its pristine stage even after 1-week duration.

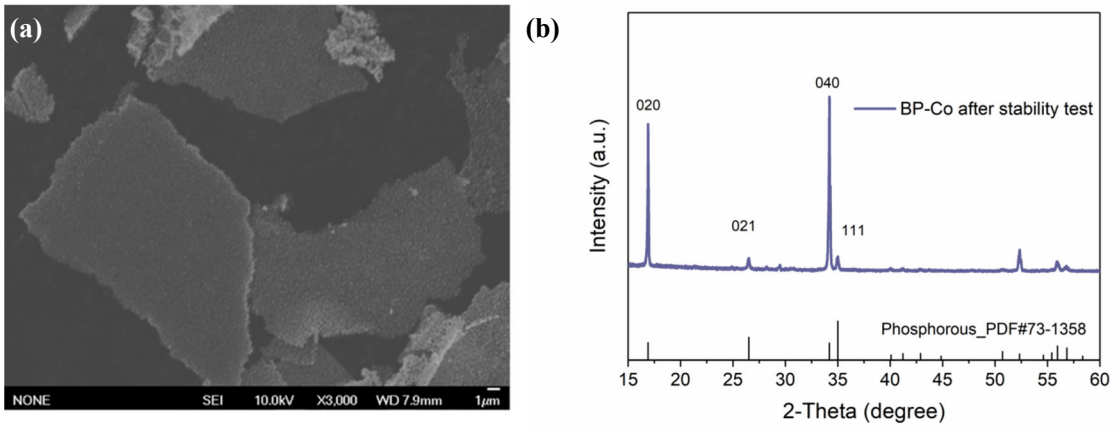

Figure S24. SEM images of BP-Co after photocatalytic stability measurement. (b) XRD of BP-Co after stability test.

SEM images (Figure S24) demonstrate the lamellar structure of BP nanosheets is preserved after 1-week stability test. The coarse surface of BP-Co is resulted from oxidation, and the small particles which can be observed are P_xO_y species as reported.[1] Meanwhile, no obvious changes can be found in XRD of BP-Co before and after stability test. Therefore, it is reasonable to believe the interaction between Co and P on the surface may slow down the degradation and improve the long-term stability of BP nanosheets.

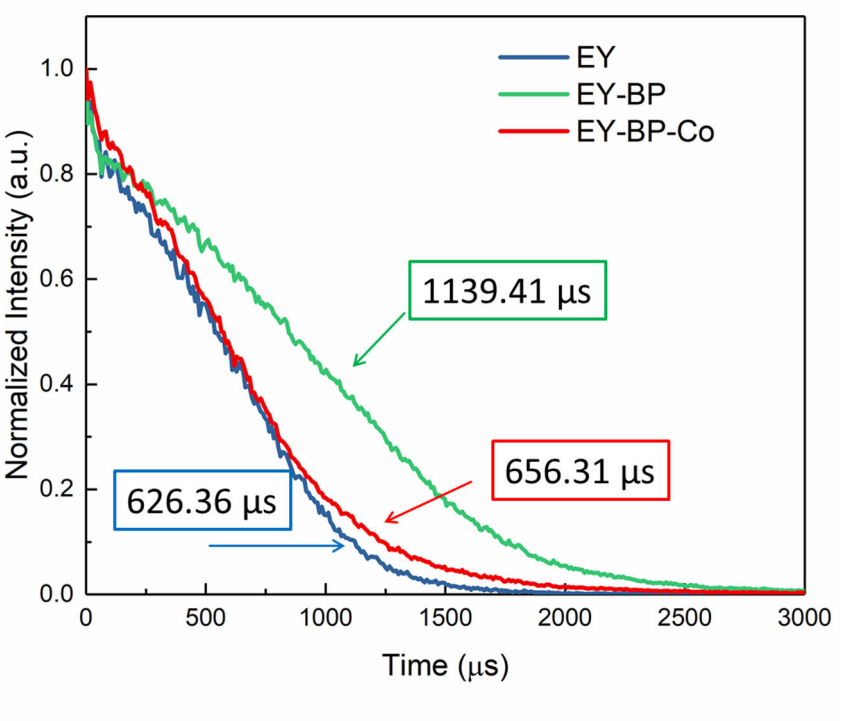

Figure S25. Time resolved photoluminescence (TRPL) decay spectra of EY, EY-BP and EY-BP-Co materials.

In addition, time resolved photoluminescence (TRPL) decay spectra (Figure S25) indicate a longer carrier lifetime of EY-BP (1139.41 μs) compared to EY (626.36 μs). The prolonged

photogenerated carrier lifetime is derived from efficient electron transfer from EY to BP, for BP nanosheets have good conductivity and suitable bandgap to help electron-hole separation. As to BP-Co, the loading of Co decrease the lifetime from 1139.41 μs to 656.31 μs, revealing new charge transfer channel to Co-P(O) active sites.

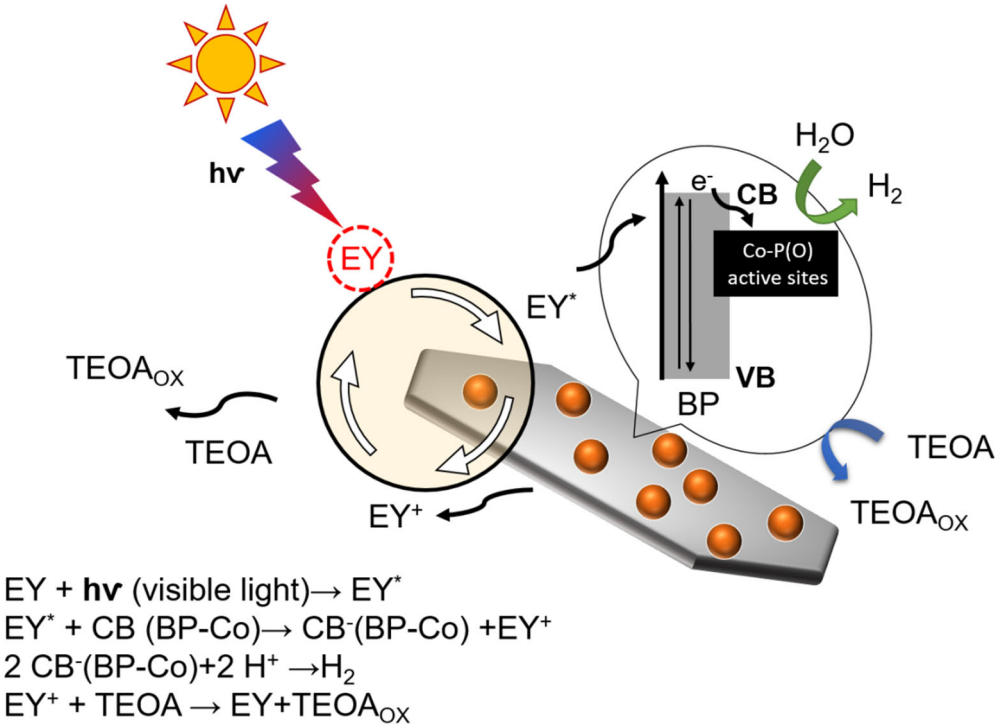

Figure S26. The schematic illustration about the mechanism of electron transfer in EY boosted BP-Co materials.

The mechanism is proposed in Figure S26. The Co-P(O) bond formation results into uniform single atom dispersion of Co on BP (BP-Co) and additional charge transfer channel, which are two key reasons for improving the H_2 photocatalytic reaction.

Table S1. Raman peak positions of BP bulk, BP nanosheets and BP-Co

	A_g^1	B_{2g}	A_g^2
BP bulk	361.4 cm^{-1}	436.6 cm^{-1}	464.4 cm^{-1}
BP nanosheets	363.4 cm^{-1}	437.5 cm^{-1}	465.3 cm^{-1}
BP-Co	360.2 cm^{-1}	432.7 cm^{-1}	460.4 cm^{-1}

Table S2. Comparison of the photocatalytic H_2 production performance between the present BP-based photocatalysts with rivaling performance in literatures.

Materials	Measurement	H_2 production	Reference
CdS-BP-Co	> 420 nm 20% lactic acid	345.4 μmol h^{-1} 17.27 mmol h^{-1} g^{-1}	**This work**
CdS-BP	> 420 nm 20% lactic acid	53.2 μmol h^{-1} 2.66 mmol h^{-1} g^{-1}	**This work**
C_3N_4-BP	>420 nm 20% methanol	0.427 mmol h^{-1} g^{-1}	JACS, 2017[2]
CdS-BP	> 420 nm 18% lactic acid	11.2 mmol h^{-1} g^{-1}	Angew. Chem., 2017[3]
CdS-BP-MoS_2	> 420 nm 18 % lactic acid	18.1 mmol h^{-1} g^{-1}	Angew. Chem., 2017[3]
BP-CdS-$La_2Ti_2O_7$ ternary composite	>420 nm Na_2S-Na_2SO_3	0.8 mmol h^{-1} g^{-1}	Applied Catalysis B: Environmental, 2019[4]

Table S3. Comparison of the photocatalytic H_2 and CO_2 production performance of BP-Co with the state-of-the-art cocatalysts in the presence of [Ru(2, 2'-bipyridy)$_3$]Cl_2 as photosensitizer.

Materials	H_2 production	CO_2 production	Reference
BP-Co	61.1 μmol h^{-1}	88.6 μmol h^{-1}	**This work**
Co-ZIF-9	59.8 μmol h^{-1}	83.6 μmol h^{-1}	Angew. Chem., 2014[5]
Co_3O_4 Hexagonal Platelets	5.95 μmol h^{-1}	20.03 μmol h^{-1}	Advanced Materials, 2016[6]
Co-C	5.22 μmol h^{-1}	9.36 μmol h^{-1}	Small, 2018[7]
Cu-based BIF-29	7 μmol h^{-1}	33.34 μmol h^{-1}	Angew. Chem., 2019[8]
NiCoOP@ carbon fibers	8.6 μmol h^{-1}	16.6 μmol h^{-1}	Angew. Chem., 2019[9]

References

[1] a) M. T. Edmonds, A. Tadich, A. Carvalho, A. Ziletti, K. M. O'Donnell, S. P. Koenig, D. F. Coker, B. Özyilmaz, A. C. Neto, M. Fuhrer, *ACS Appl. Mater. Interfaces* **2015**, *7*, 14557-14562; b) J. D. Wood, S. A. Wells, D. Jariwala, K.-S. Chen, E. Cho, V. K. Sangwan, X. Liu, L. J. Lauhon, T. J. Marks, M. C. Hersam, *Nano Lett.* **2014**, *14*, 6964-6970.

[2] M. Zhu, S. Kim, L. Mao, M. Fujitsuka, J. Zhang, X. Wang, T. Majima, *J. Am. Chem. Soc.* **2017**, *139*, 13234-13242.

[3] J. Ran, B. Zhu, S. Z. Qiao, *Angew. Chem. Int. Ed.* **2017**, *56*, 10373-10377.

[4] L. Mao, X. Cai, S. Yang, K. Han, J. Zhang, *Appl. Catal. B* **2019**, *242*, 441-448.

[5] S. Wang, W. Yao, J. Lin, Z. Ding, X. Wang, *Angew. Chem. Int. Ed.* **2014**, *53*, 1034-1038.

[6] C. Gao, Q. Meng, K. Zhao, H. Yin, D. Wang, J. Guo, S. Zhao, L. Chang, M. He, Q. Li, H. Zhao, X. Huang, Y. Gao, Z. Tang, *Adv. Mater.* **2016**, *28*, 6485-6490.

[7] K. Zhao, S. Zhao, C. Gao, J. Qi, H. Yin, D. Wei, M. F. Mideksa, X. Wang, Y. Gao, Z. Tang, R. Yu, *Small* **2018**, *14*, 1800762.

[8] H. X. Zhang, Q. L. Hong, J. Li, F. Wang, X. Huang, S. Chen, W. Tu, D. Yu, R. Xu, T. Zhou, J. Zhang, *Angew. Chem.* **2019**, *131*, 11878-11882.

[9] Y. Wang, S. Wang, X. W. Lou, *Angew. Chem. Int. Ed.* **2019**, *58*, 17236-17240.